Shallow reflection seismic evidence of tectonic activity in the Cheb Basin, NW Bohemia

FELIX HALPAAP[1,2], MARCO PASCHKE[1] AND FLORIAN BLEIBINHAUS[1,3]

1 Institute of Geosciences, Friedrich-Schiller-University, Jena, Germany

2 now at Department of Earth Sciences, University of Bergen, P.O.Box 7803, Bergen 5020, Norway (felix.halpaap@uib.no)

3 now at Chair of Applied Geophysics, Montanuniversitaet Leoben, Leoben, Austria

Received: September 5, 2016; Revised: February 10, 2017; Accepted: March 26, 2017

ABSTRACT

With a high-resolution seismic survey, we targeted the shallow structural features of the Cheb Basin, Northwest Bohemia. The aim of this study was to evaluate these features' relation to seismic activity below the Cheb Basin with the first reflection seismic image of parts of the basin. We recorded a densely sampled, 3200 m long seismic survey stretching from Kopanina towards SE, into the basin. From the recordings of 170 shots at 192 geophones with 384-m total spread, we obtained a reflection seismic image down to the basement at 300-m depth, supplemented by a shallow tomographic velocity model for the uppermost 40 m. Strong lateral velocity contrasts indicate Quaternary river terraces, into which the Plesná river incises. We observe reverse faults in the lower basin sediments, which we interpret as signs of a push-up structure related to the N-S oriented Počátky-Plesná Zone (PPZ). However, we do not observe any vertical fault offsets in the younger sedimentary layers, which suggests that any normal or reverse faulting must be older than 20 Ma. The image agrees well with previous lithostratigraphic borehole data and previous sedimentological and tectonic models. Our explanation for the formation of the escarpment at the eastern bank of the Plesná valley, previously interpreted as outcrop of the PPZ, relies solely on incision of the Plesná river into weak sediments.

Keywords: Cheb Basin, seismic reflection survey, Mariánské Lázně Fault, Počátky-Plesná Zone, first arrival traveltime tomography

1. INTRODUCTION

The Cheb Basin in Northwest Bohemia (see Fig. 1) exhibits unique geological features such as earthquake swarms (e.g., *Fischer et al., 2014*), wet and dry mofettes which emanate CO_2-rich, mantle-derived gas (e.g., *Bräuer et al., 2008*) and Quaternary volcanoes (e.g., *Mrlina et al., 2009*). High-resolution relocation of earthquakes through the master event procedure shows that the swarms occur on planar features below Nový Kostel (*Fischer and Michálek, 2008*). Two major faults in the area have been identified: The Mariánské Lázně Fault (MLF), which clearly marks the eastern margin of the Cheb

Stud. Geophys. Geod., 62 (2018), 80–101, DOI: 10.1007/s11200-016-0386-7

Basin, and the Počátky-Plesná Zone (PPZ) which *Bankwitz et al. (2003b)* proposed. The PPZ's strike is supposed to match exactly the strike of the plane outlined by earthquake swarms (*Fischer et al., 2010, 2014*), while the MLF strikes at an angle differing by ≈15°, further NNW-SSE. This also places the PPZ in line with the mofette field Milhoštov-Hartoušov, which lies 4 km south of this seismic survey (*Bankwitz et al., 2003b*; *Nickschick et al., 2015*).

Bankwitz et al. (2003b) interpreted the PPZ's surface outcrop at the eastern escarpment of the Plesná river based on river drainage patterns and the distribution of Quaternary sediments, but this feature is far less prominent in comparison to the MLF. Remote-sensing studies (*Peterek et al., 2011*) and the interpretation of electrical resistivity tomography images (*Flechsig et al., 2010*) supported this finding. Except for selective boreholes, all studies within the Cheb Basin recovered only shallow information which leaves an imaging gap between the shallowest 60 m and the earthquake hypocenters at 6-km depth. In the literature, the PPZ is usually suggested as the main fault which is seismically active during the earthquake swarms below Nový Kostel. However, at a constant dip of 70° to 80° reported from the alignment of hypocenters (*Fischer et al., 2014*), the seismically active Nový Kostel fault would crop out about 3 km east of the MLF at Kopanina. Thus, the connection between shallow fault expressions and structures at depth is still enigmatic, especially the relation between the Nový Kostel fault and the PPZ.

The closest previous reflection seismic survey is the SSW-NNE striking Münchberg-Vogtland-Erzgebirge (MVE) deep seismic profile, which is located ≈ 20 km north of Nový Kostel (*DEKORP Research Group, 1994a,b*). A pre-stack migration image of the MVE survey by *Bleibinhaus et al. (2003)* revealed two steeply dipping crustal faults approximately cross-cutting the WSW-ENE survey line. If the seismically active Nový Kostel Fault and the MLF are prolongated towards the North at constant strikes of 169° and 150°, respectively (*Bankwitz et al., 2003b*), then they fit the two large observed faults in the MVE survey well, where they were imaged at a dip of 65° and 57°, respectively.

To image sedimentary layers, including offsets that appear due to tectonic activity, the reflection seismic method has proven to yield the highest resolution images. However, no such survey had been conducted within the basin before. At the proposed location of the PPZ, *Bankwitz et al. (2003b)* assumed an offset of about 15 m in sedimentary layers, relying on the 25-m escarpment. Even if the dominant faulting type of the PPZ is strike-slip, we would still expect some disturbance of reflectors due to the normal faulting component and the contrast between neighboring units. In the case of pure strike-slip, displaced units would likely still produce some contrast due to inclined layers, a common feature in the Cheb Basin, or a fault plane reflection from brecciated material.

In this study we present the results of the first seismic reflection survey in the Cheb Basin, more precisely at its eastern margin, close to where the MLF and the PPZ supposedly intersect. The SW-NE oriented survey was 3.2 km long, and we recorded a total of 170 shots at 192 receivers with 2-m spacing. Our motivation was to image the internal structure of the Cheb Basin, aiming to connect local tectonic features to the large-scale structures in this geodynamically active area. We placed a special emphasis on defining the shallow tectonic expression of the PPZ and the MLF inside the basin. To resolve structure in the shallowest sediments, we obtained a P-velocity model of the

uppermost 40 m with first arrival traveltime tomography. The reflection image resolves reflectors down to the basin floor at 200-m to 300-m depth and shows both normal and reverse faulting of the sedimentary layers.

2. GEOLOGIC OVERVIEW

The Cheb Basin is a relatively small, ≈ 20 km by 10-km wide, young intracontinental basin which covers the northwestern part of the Bohemian massif (*Malkovský, 1987*), as is shown in Fig. 1. It is situated in the western part of the Cenozoic Eger Rift, at the intersection of the SW-NE striking Eger Graben and eastwards bounded by the crustal-scale, NNW-SSE striking Mariánské Lázně Fault. The Eger Rift opened as part of the European Cenozoic Rift System during post-alpine crustal extension (*Weinlich et al., 2006*). The basin covers Paleozoic Variscan units and post-Variscan granites (*Schunk et al., 2003*) and is seated above the crustal triple junction of three ancient microcontinents which *Babuška et al. (2007)* outlined from variations in the crustal seismic anisotropy.

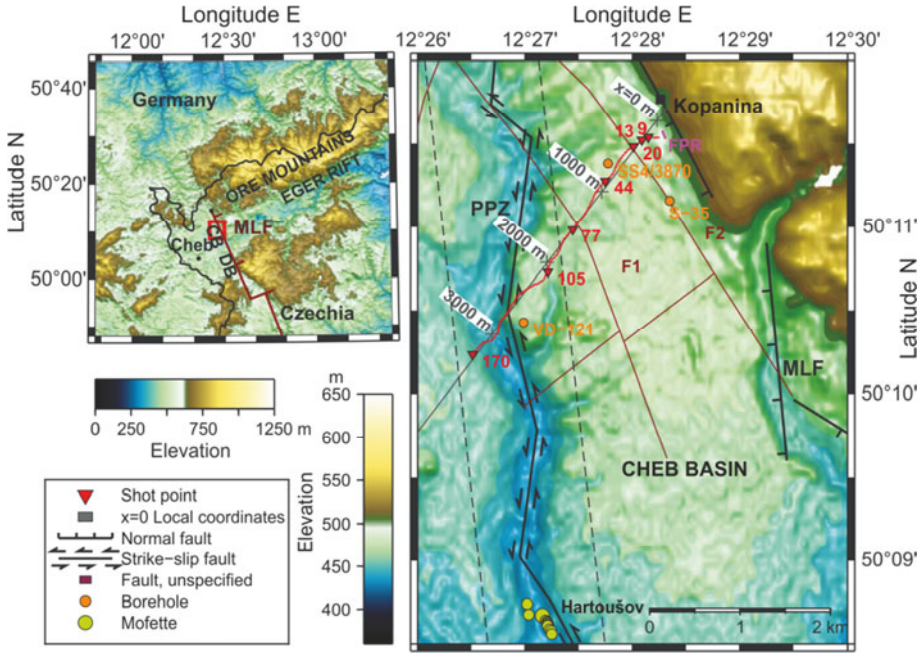

Fig. 1. The topographic overview map on the left shows the location of the Cheb Basin (CB) and the Domažlice Basin (DB) in Western Bohemia and their relation to the Eger Rift and Ore Mountains. Marked with a red rectangle is the location of the enlarged topographic map on the right which shows the northern Cheb Basin. It includes fault lines based on *Bankwitz et al. (2003a)* in black and faults without indications of shear sense based on *Škvor and Sattran (1974)* and *Emmert et al. (2007)* in dark red. MLF: Mariánské Lázně Fault, PPZ: Počátky-Plesná Zone, FPR: fault plane reflection, imaged through prestack migration. Wet mofettes of the Milhostov-Hartoušov field located by *Nickschick et al. (2015)* are marked in turquoise.

2.1. Local tectonics

The fault which is most often referred to as being seismically active during the earthquake swarms is the Počátky-Plesná Zone (PPZ), first suggested by *Bankwitz et al. (2003a)*. They supposed the fault's outcrop to be visible at the eastern flank of the Plesná river valley, from which they coined the fault's name. Their definition of the surface location is based on geological and geomorphological field observations and satellite observations, mainly the Plesná river's drainage pattern and its changes over time. At a strike of 169°, the PPZ is clearly differentiated from the better known crustal-scale Mariánské Lázně Fault (MLF), which strikes at 150°.

The extent of neither the seismically active fault nor the PPZ are clearly known, because they do not form a clear surface structure in comparison to the MLF. North of the Cheb Basin, *Bleibinhaus et al. (2003)* imaged a fault dipping at 65° close to the village of Falkenstein by reprocessing the Münchber-Vogtland-Erzgebirge active seismic survey data. This location is in line with the seismically active fault when extending the fault's strike northward from the Nový Kostel focal zone. South of the focal zone, the mofette field Milhostov-Hartoušov is located in approximate southward continuation of the focal zone (see Fig. 1). Several authors (*Bankwitz et al., 2003b*; *Fischer et al., 2014*; *Nickschick et al., 2015*) have pointed out that the mofettes and the large-scale fault structures are likely connected. *Nickschick et al. (2015)* found that degassing occurs only west of a N-S striking morphological step which likely marks the PPZ at the surface. These northern- and southernmost PPZ-related observations would imply a minimum length of 50 km for the PPZ.

The main boundary fault of the Cheb Basin is, however, the MLF, which controls the basin's formation on its eastern margin (*Špičáková et al., 2000*). The MLF is 150 km long (*Peterek et al., 2011*) and crosscuts the Eger Rift in its northern part, where the fault forms the topographically most noticeable tectonic feature. To the west of the Northern MLF, the Cheb-Domažlice Graben strikes NW-SE, while the Eger Graben extends in northeastern direction from the MLF (see Fig. 1). At this location, which today is marked as the intersection of the two grabens, the Cheb and the Domažlice basins formed. Subsidence of the whole Eger Rift started in late Oligocene and continued until early Miocene (*Špičáková et al., 2000*). From mid-Miocene onward, the Eger Graben was uplifted, while subsidence in the Cheb Basin resumed in late Pliocene due to the development of the Cheb-Domažlice Graben. The formation of the Cheb-Domažlice Graben, and hence the Cheb Basin, is bound to activity along the MLF (*Peterek et al., 2011*).

Within the basin, sedimentary overprint makes faults hard to track at the surface. *Škvor and Sattran (1974)* located several smaller scale faults around the Plesná river (see "F1" and "F2" in Fig. 1). *Špičáková et al. (2000)* state that the current structure of the basin is strongly affected by reactivation of the MLF during the Quaternary, which led to the formation of horsetail-splays at its northern termination. These horsetail splays are made up of oblique extensional faults striking parallel to the MLF or westwardly deviated from it. The horsetail-splays are an expression of a shift of the main stress axis from a N-S trend to NNW-SSE, causing sinistral strike-slip activity along the MLF. *Peterek et al. (2011)* inferred changes in the Quaternary drainage pattern from incisions in the

shallowest sediment layers. They present these changes as an important argument for the existence of recent fault activity in the Cheb Basin.

2.2. Stratigraphy

Sediments deposited during the extensional periods are mostly of Miocene and Quaternary origin, and they show strong local thickness variations in the Cheb Basin. *Špičáková et al. (2000)* compiled a comprehensive borehole dataset of the Cheb basin in a 3-D model and showed that the basin deepens towards the MLF in the northeast. Sedimentation in the basin was not continuous, so that partial uplift and erosion of the basin's margins, e.g., between Miocene and Pliocene, resulted in major unconformities.

Our survey is situated about 2 km north of the basin's largest sediment thickness of 300 m according to their model. Two boreholes (SŠ-4 and 3870) are in close proximity to our survey line (25 m) and to the MLF, and corresponding borehole logs are published in the GEOFOND database of the Czech Geological Survey (*Šantrůček, 1956*; *Plaček, 1966*). Their logs contain estimates of layer thickness and visual descriptions of grain size and sediment color and dominant portions of limestone or coal are indicated. While the boreholes themselves are less than 20 m apart, the reported depths to the basement, 277 m for SŠ-4 and 267 m for 3870, vary significantly, as well as the level of detail at which layers were reported. For SŠ-4, the 123 minor layers in three units often vary little and are described for 1m to 3m thickness on average, while the log for 3870 mentions 24 minor layers in four units with on average 10-m thickness. Of the strata unveiled in the boreholes, only the younger strata, namely Quaternary sediments and the Vildštejn Formation (Fm.) are exposed at the surface.

Besides the borehole data, only shallow geophysical imaging studies have recovered subsurface structure in the basin, e.g. a 2-D ground penetrating radar (GPR) study by *Hubatka et al. (2004)*, a small-scale 3-D GPR by *Fischer et al. (2012)* and an electric resistivity tomography study by *Flechsig et al. (2010)*. According to *Bankwitz et al. (2003a,b)*, the main aquifer inside the Cheb Basin is located below the Vildštejn Fm. A blow out of 50-m height at borehole H11 near Františkovy Lázně proves that the fluid is under constant high pressure (*Kolářová, 1965*), most likely supported by the continuous ascension of gas.

Špičáková et al. (2000) devised three major depositional periods in the basin (see Table 1), which were mostly dated from plant fossils and pollen. Table 1 summarizes reflector depths estimated within this study, the associated boundary and sedimentation interval and the lithology of intervals reported in the borehole logs for SŠ-4 and 3870.

Interval I lasted from 35 to 21 Ma and resulted first in fluvial sedimentation of the Lower Clay and Sand Fm. and the succeeding Main Coal Seam Fm. between approximately 26 and 21 Ma. Deposition of the lower formation, which consists of sand, gravel and kaolinitic clay, coincided with the main volcanic phase of the volcanoes of Železná hůrka (ZH) and Komorní hůrka, which are located at the southwestern margin of the Cheb Basin (*Mrlina et al., 2009*). In the Main Coal Seam Fm., deposition of clay and organic material in a mire environment resulted in coalification of associated layers. Sediments of these formations are concentrated in localized depocenters, with the largest one situated adjacent to the MLF. *Špičáková et al. (2000)* report a maximum thickness of 30 m for the Interval I deposits.

Table 1. Main sedimentation intervals and their seismic reflectors. Reflector depths stem from this seismic survey, interval definitions and their timing from *Špičáková et al. (2000)* and the described lithologies from logs of two boreholes (*Šantrůček, 1956*; *Plaček, 1966*).

Top Reflector Depth [m]	Interval	Period [Ma]	Main Lithology	
			SŠ-4	3870
3	III. Vildštejn Fm.	4.5–1.5	loam	clayey loam
110	II. Cypris Fm.	21–17	clayey slate	bedded clay
220	I. Coal Seam Fm.	26–21	coal	firm coal
240	I. Lower Clay and Sand Fm.	35–26	carbonaceous clay, clayey sand	carbonaceous clay, kaolinitic granitic sand
280	Smrčiny Mts. Pluton		granitic sand	decomposed granite

Interval II was sedimented between 21 and 17 Ma, and a flooding surface marks the boundary towards Interval I. Lacustrine deposition of clayey sediments occurred in the whole basin, especially in alluvial fans. Sediments accumulated with 70 to 120-m maximum thickness at the basin's northwestern margin in proximity to the MLF, thinning towards the west (*Špičáková et al., 2000*). The end of NW-SE extension of the Eger Graben between 24 and 16 Ma (*Adamovič and Coubal, 1999*) coincides with the lack of sediments deposited between 16 and 5 Ma in the Cheb Basin. *Špičáková et al. (2000)* connect the absence of sediments with tectonic uplift and erosion of marginal parts of the Eger Graben, especially the Bohemian Massif north of the Cheb Basin. *Adamovič and Coubal (1999)* further infer a compressional phase, accompanied by erosion, between 16 and 12 Ma.

Interval III, which lasted from 4.5 to 1.5 Ma, is marked by an unconformity separating sediments with 12 My difference in age towards the second interval. This third interval is made up of the Vildštejn Fm., which was deposited fluvially and in alluvial fans between 4.5 and 1.5 Ma. The top of the formation is the present-day erosional surface, or the base of the Quaternary deposits (*Špičáková et al., 2000*). Deposition of fluvial gravel, sand and kaolinitic clays once again concentrated in fluvial, floodplain and alluvial facies in the main depocenter close to the MLF. Uplift of the basin in the Quaternary led to erosion and further incision of rivers, which formed erosional terraces (*Schunk et al., 2003*). In mid-Pleistocene, the 420–781 ka old Milhostov Fm., which overlays the Vildštejn Fm. discordantly, was deposited (*Bucha et al., 1990*).

3. METHODS: DATA ACQUISITION AND PROCESSING

We acquired a densely sampled seismic survey, stretching from Kopanina at the MLF, southeast of Nový Kostel, in SW direction, 3200 m towards the basin interior. It thus covers the eastern part of the Cheb Basin including the Plesná river valley, where *Bankwitz et al. (2003b)* suspected the terrain escarpment at the eastern valley flank to be an outcrop of the PPZ. The survey line, shown in Fig. 1, spreads approximately perpendicular to these expected structural features along a minor rural road, where we

could avoid recording close-by traffic noise during the periods of shooting. We recorded 170 shots, each spaced at 20 m, at 192 single receivers with 2-m spacing intervals. By placing geophones in this dense fashion, we assured to get complete records of the surface waves for further analysis and to avoid spatial aliasing of higher frequencies. We used the recorded data for first arrival traveltime tomography (Fig. 3) and reflection seismic imaging (Figs 4–6).

For each shot location, we recorded the position by differential GPS measurements with a precision of a few centimeters. We transformed the recorded locations to a local right-handed coordinate system $\{x', y', z'\}$, where the x' axis is pointing towards 230.5°N (see Fig. 1). This is the best-fit through all shot points in survey direction, with the origin of x', y', z' located 100 m northeast of shot point 3. As signal sources we employed a Geosym Seismic Impulse Source System (SISSy) to fire 8 g propellants in 1-m deep boreholes (*http://www.geosym.de/assets/Uploads/FlyerSISSYGB.pdf*). Employing these small amounts of explosives transfers a significant amount of high-frequency energy, which helps to increase the resolution of a small-scale survey.

Of the geophones deployed, one half had a corner frequency of 10 Hz, the other half 4.5 Hz, as Fig. 2a shows on the mean amplitude spectra of all traces. Hence, we corrected the traces recorded by 10-Hz geophones to match the instrument response of the 4.5-Hz geophones through filtering in the time domain. For this instrument simulation (*Scherbaum, 2001*), we first created a frequency domain filter based on the ratio of measured frequency response functions of the 4.5-Hz and the 10-Hz geophones (see Fig. 2b) for the geophone and filter amplitude spectra and Fig. 2c for their phase spectra). Then, we converted this filter to the time domain and convolved it with the traces recorded by 10-Hz geophones, equalizing the recordings of all geophones (see restituted spectrum in Fig. 2a).

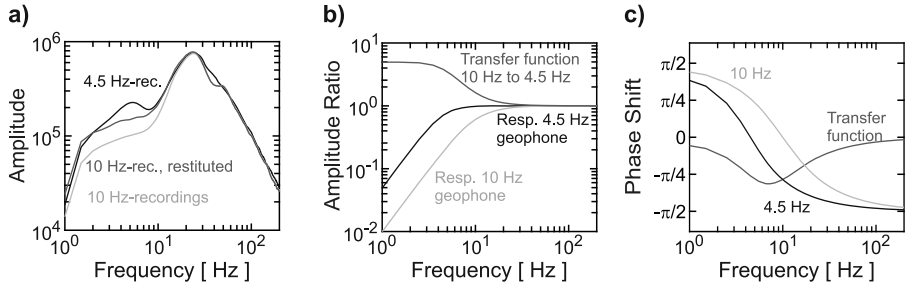

Fig. 2. Frequency content of the recordings and instrument simulation filter. **a)** Average amplitude spectra of all traces recorded by the 4.5 and 10-Hz geophones, and the spectrum of the 10-Hz geophone recordings after restitution to 4.5-Hz geophone recordings. **b)** Instrument's amplitude responses for 4.5 and 10-Hz geophones, and the response of the filter used to restitute the recordings. **c)** Phase responses for geophones and filter.

3.1. Data quality

Noise content, including surface and shear waves, varies considerably between shot gathers. Figure 4a shows three data examples from shot points 44, 77 and 105, which are marked on the map in Fig. 1. These gathers hint to a trend of stronger surface wave propagation further inside the basin. The main reflections at 0.2–0.3 s are partly concealed by both S-waves and clearly dispersive surface waves. Even though we avoided close vehicle traffic in the recordings, some coherent noise from distant sources, possibly agricultural vehicles, occurs in the data. Coherent noise thus covers a wide range of propagation velocities between 150 and 800 m s^{-1}, which required filtering.

3.2. First arrival traveltime tomography

The goal of first arrival traveltime tomography (FATT) was to obtain a near-surface velocity model for static corrections, and to recover structural features that would be too shallow to be imaged by reflection seismic processing. We inverted 27354 manually picked first arrival times for the shallow P-velocity structure in 2.5-D along the survey line. Here, 2.5-D means that we calculated the forward solution by solving the eikonal equation in 3-D, honoring the crookedness of the survey, while only allowing 2-D variations in structure during the inversion. We used the SIMULR16 code (*Bleibinhaus, 2003*), which is an upgraded version of the well-known SIMULPS local earthquake tomography code (*Thurber, 1983*; *Eberhart-Phillips, 1990*; *Thurber and Eberhart-Phillips, 1999*) that uses an eikonal solver to compute time fields and rays. SIMULR16 employs a damped least-squares inversion to compute model perturbations of an initial velocity model that reduce the residual while keeping the perturbations as small as possible. The damping factor that weighs the perturbation size relative to the residuals was estimated from an L-curve test. To account for the non-linearity, the inversion is iteratively repeated. The iterative update in model parameters $\Delta\boldsymbol{m}$ for an initial model $\boldsymbol{m}$ can be described as:

$$\Delta\boldsymbol{m} = \left(\mathbf{G}^{\mathrm{T}}\mathbf{G} + \Theta^2\mathbf{E}\right)^{-1} \times \left(\mathbf{G}^{\mathrm{T}}\Delta\boldsymbol{d}\right), \tag{1}$$

where $\mathbf{G}$ is the data kernel, Θ is the damping parameter, $\mathbf{E}$ is the identity matrix and $\Delta\boldsymbol{d}$ is the residual between the current model's synthetic traveltimes and the traveltime observations $\boldsymbol{d}$.

The inverse model is defined on a rectangular grid with bilinear interpolation. To locally adapt the grid node density to the ray path density, grid nodes can be removed from the inverse grid, and the corresponding velocity is interpolated from the nearest neighbors. Close to the surface, we aimed for a higher resolution according to the highest present frequencies and the receiver spacing. At depth, only a few nodes are inverted. The *x* axis of the grid is oriented with a slight dip in relation to the surface to honor the gentle dip towards the center of the basin. Realistic solutions rely on an educated guess for the initial 1-D velocity model, which we obtained from analyzing the apparent velocities of the first arrivals. The final velocity model is displayed along with the inverted node position in Fig. 3. This final model resulted from the third iteration, where the residual dropped below our termination criterium of 5 ms, equal to the assumed picking error.

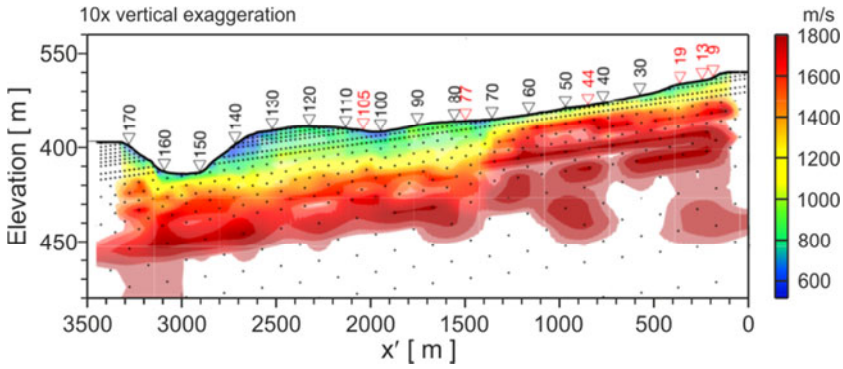

Fig. 3. Shallow P-velocity model from tomographic inversion, superimposed with the rotated inversion grid. Color intensity is scaled by the diagonal elements of the resolution matrix, noting how independently and well defined the solution is at each inversion node. The inversion grid's density decreases with depth. The result is based on an initial 1-D velocity model with constant gradient.

3.3. Reflection seismic processing

We followed a standard post-stack migration processing scheme for the whole survey, which we supplemented with a prestack migration image of a single steeply dipping reflector that appeared nearby the MLF. The most crucial poststack processing steps were the surface wave filtering, normal move-out correction (NMO), the construction of a realistic velocity model and detailed static corrections. We utilized Seismic Unix 43R1 (*Stockwell and Cohen, 2008*), whose advantage over reflection processing programs designated for industry is a great flexibility in importing information, for example externally calculated static corrections and velocity models.

Trace and amplitude corrections

We corrected the polarities of 43 traces which resulted from faulty connected geophones and muted another 278 traces. These showed either a monofrequent signal, no phase correlations to the neighboring traces or strong noise. We applied static corrections considering receiver and shot elevations and the weathering layer, which we defined arbitrarily as the layer above the isoline of 1200 m s^{-1}. To minimize the required correction values, we chose a dipping reference datum which follows the topographic trend along x' at –0.8°. We extracted thickness and velocity structure of the weathering layer from the tomographic P-velocity (v_P) model. Then, we corrected traces by the difference between the vertical traveltime in the weathering layer based on the 2.5-D velocity model and the traveltime in a homogeneous layer with v_P = 1200 m s^{-1} and the same thickness. We corrected amplitudes for spherical divergence according to a 1-D root-mean-square (*RMS*) spreading velocity function $v_{RMS}(t)$ based on the average of the 2-D stacking velocity model $v_{st}(x,t)$ (generation of the 2-D stacking velocity model

is described in Section "Velocity model construction and poststack migration"). Even though an automatic gain control (AGC, here with 0.2-s window length) destroys relative amplitude information (*Sheriff and Geldart, 1995*), it was crucial to attenuate dip filtering artefacts and surface waves, which were up to 100 times stronger than reflections. These first processing steps have been applied to the sample shot gathers shown in Fig. 4a). Note the complete disappearance of reflections after the surface wave arrival which gives an idea of the true amplitude ratios.

Deconvolution and frequency filtering

Gapless spiking deconvolution (*Yilmaz, 2001*), with a maximum lag equal to the width of the main peak of the autocorrelation function reduced the source ringing and whitened the spectrum. We applied a 15 to 140-Hz bandpass filter (frequencies completely muted below 10 Hz and above 160 Hz), basing the lower corner frequency on the amplitude drop-off in the spectrum (see Fig. 2a). Against expectations (*Yilmaz, 2001*), high frequencies up to 140 Hz, our upper corner frequency, contained reflection signal. This high frequency content proved that using small amounts of explosives for a survey of comparable size is very suitable to achieve the highest possible resolution. Corresponding with our maximum expected basement depth of ≈ 300 m according to the logs for boreholes SŠ-4 and 3870, we saw the latest reflections at ≈ 0.35 s two-way time (TWT). We attenuated earlier multiples with a predictive error filter with a minimum lag of 80 ms to reduce ringing further. The deconvolved and filtered shot gather samples are shown in Fig. 4b.

Surface and S-wave filtering

A slant stack dip filter in the τ-p domain as described by *Yilmaz (2001)* for ray parameters between $p = 0.001$ and 0.005 s m^{-1} gave best results to filter out surface waves and direct P and S-phases. Due to the dense receiver spacing, we could avoid spatial aliasing for surface wave phases of 200 m s^{-1} with up to 200 Hz at a resolution limit of 10 ms per trace. Afterwards, we scaled trace amplitudes for systematic variations by receivers and shots to eliminate coupling-dependent variations. With the traditional common mid point (CMP) definition with one CMP every halfed receiver spacing (*Yilmaz, 2001*), the median fold is only ten at 2-m spacing for 192 receivers and 20-m spacing for 170 shots, but the fold varies for each mid point depending on when the survey was rolled forward.

Stacking on average ten traces returned rather low-quality stacks, for which reason we decided to bin traces of neighboring common mid points of 8 m along the survey together, effectively reducing the number of common mid points and increasing the fold. For this binning we considered the exact mid point between sources and receivers along a crooked line, which resulted on average in 76 traces per mid point bin. The CMP bin size of 8 m is optimal in consideration of the Fresnel zone size and spatial aliasing during poststack processing. With the 8-m bins, even shots around shot point 77 produce visible reflectors, even though reflection amplitudes are weak in this area compared to the beginning of the survey (compare raw data in Fig. 4).

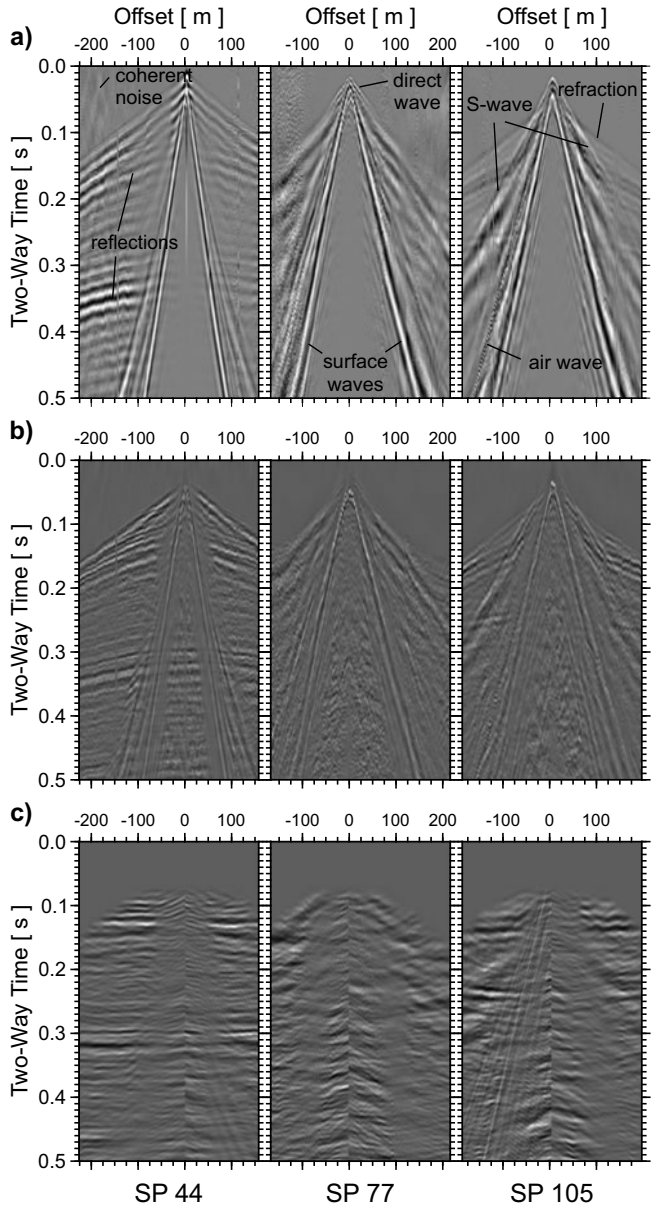

Fig. 4. Data samples of the poststack reflection processing. **a)** Example shot gathers (SP 44, 77, 105) with corrected statics and balanced by trace amplitude. Distinct wave phases and noise types are marked, and noise content clearly varies across the line. **b)** Deconvolved and filtered shot gathers, **c)** dip-filtered and normal move-out corrected shot gathers. The τ-p filter produces some artifacts near zero offset that, however, are of little impact after stacking.

Velocity model construction and poststack migration

We derived a stacking velocity model by picking velocities on semblance plots and constant velocity stacks in three cycles, using scripts from *Schleicher (2012)*. Our stacking velocity model changes slightly along the survey and is usually defined by three to five picks per CMP gather, typically one pick per main reflector. Between each picking cycle, we calculated surface consistent residual statics by stack power maximization (*Ronen and Claerbout, 1985*) through which reflections stacked better and appeared flatter on a small scale. Based upon the width of semblance peaks and trial runs, we estimate our velocity picking error between 5% and 20%. Dip-filtered and NMO-corrected sample shot gathers are shown in Fig. 4c).

Depth migration requires a model of the interval velocities in each layer, which we calculated from the picked stacking velocities (assumed equal to *RMS*-velocities due to horizontal layering) with Dix's equation (*Dix, 1955*). For the shallow subsurface, we could directly integrate the higher resolution tomographic velocity model into the interval velocity model. Below the area of tomographic coverage, we simplified the model to three main layers, one above the main mid-basin reflector, one down to the basement and one as basement. Due to the rather simple geology of subhorizontal reflectors, we assumed that the velocity model was accurate enough for poststack depth migration. We applied Fourier finite-difference poststack depth migration (*Ristow and Rühl, 1994*) which combines the advantages of *f-k* domain migration (mapping of steep dips) and finite difference migration (consideration of heterogeneous velocity distributions). The resulting section after migration is shown in Fig. 6a.

3.4. Prestack migration of a fault plane reflection

We assumed to cross tectonic structures approximately perpendicular along the survey line, but the survey design was dictated by the availability of backcountry roads. To test if the 3-D structure, e.g. along the MLF, affected our recordings, we checked the data for possible out-of-plane reflections and performed prestack migration. Due to poor accessibility, we did not record shots across where *Bankwitz et al. (2003a)* allocated the MLF, which would have required laying out the survey across the busier road 212 in Kopanina. In addition, we lost recordings of the first two shot points in Kopanina. However, due to the bending of the survey road in Kopanina, we obtained some 3-D coverage of this structurally challenging location, where we were thus able to perform prestack migration in 3-D. Further within the basin, we expect the assumption of 2-D structures to be more robust. The latest reflections of the whole survey arrive at 0.35 s TWT, which means that any reflections from the MLF could only have an effect on the recordings within a distance of 300 m of the fault.

Some shot gathers obtained close enough to the basin's margin (e.g. 9, 13, 19, see Fig. 1) showed reflection hyperbolas with their apex shifted towards the MLF and clearly outside the imaged area below the receivers (see Fig. 5a). We suspected these to be reflections from a steeply dipping fault plane (*Hole et al., 1996*) whose imaging requires prestack migration methods (*Bancroft, 2007*). We chose to apply 3-D Kirchhoff prestack depth migration, implemented in the code kirch2B written by David Okaya (*Hole et al., 2001*). This allowed us to take the particular geometry at the beginning of the survey into

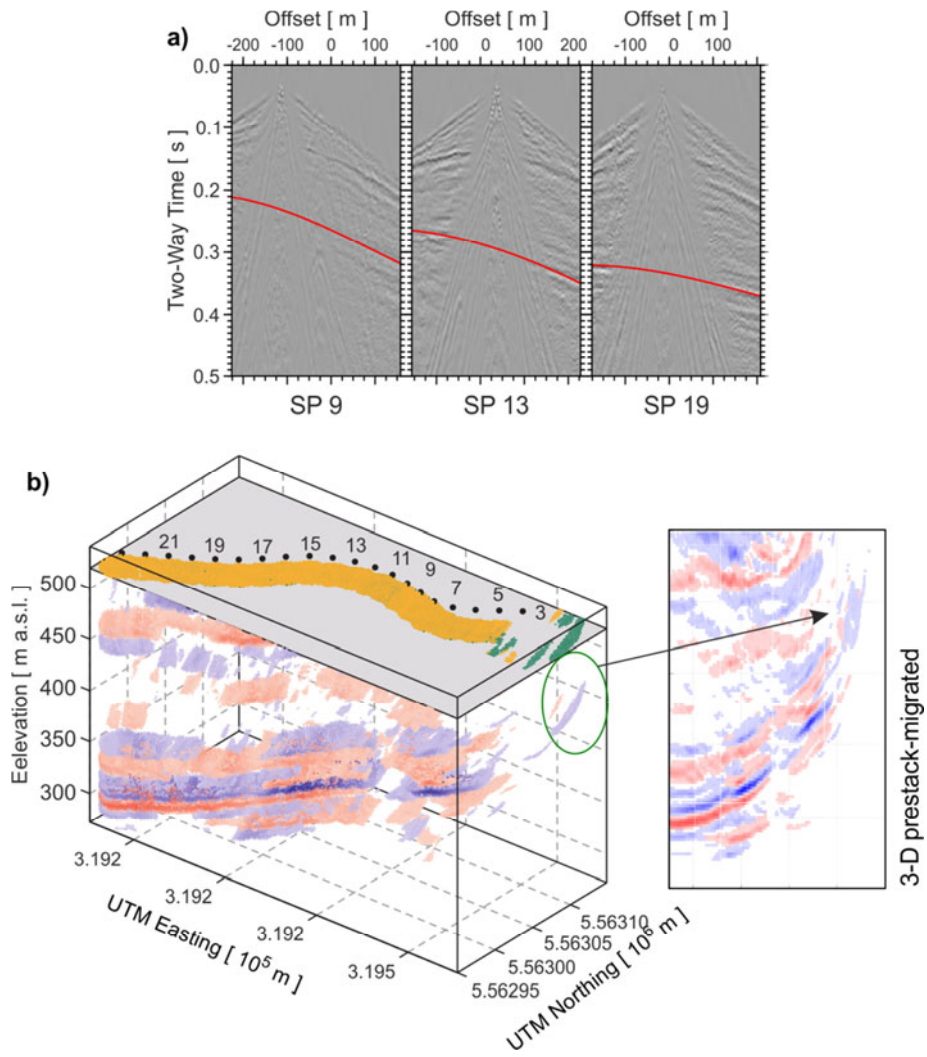

Fig. 5. Prestack processing of a steeply dipping reflector. **a)** Shot gathers 9, 13 and 19, showing reflection hyperbolas with their apex shifted towards the east, possibly from a reflector outside the survey spread. **b)** The reflections migrated through 3-D prestack Kirchhoff migration in a data cube. The figure shows signal above an arbitrarily selected threshold to show migrated reflectors within the cube, and the width of reflectors perpendicular to the survey line limited to suppress migration artefacts.

account, where the survey line curves considerably and runs towards the MLF at an angle of 70° between survey direction and suspected MLF strike.

Our tests showed that finding steep reflections in 3-D migrated 2-D line data is challenging, because of the strong artefacts of layer reflections that arise parallel to the

survey line, along hyperbolas perpendicular to the survey (these parallel artefacts from are already muted in Fig. 5b,c). These artefacts are purely a consequence of the 2-D coverage. Imaging reflectors is thus only possible in areas around the tip of the 2-D profile, where our survey could record some reflections in 3-D. At the survey's tips, reflections from horizontal layers additionally stack worse than they do on flanks of a semi-circle parallel to the survey line. To avoid some of these artefacts, we muted the input traces after the latest visible reflection signals. We applied no taper to the traces at the top as our goal was to image a very steep structure, and we chose a spatial sampling of 2 m in x, y, and z direction. The pseudo-3-D velocity model extended the 2-D model (the combination of tomographic velocity model and interval velocities) in parallel to the strike of the MLF, while we chose a homogeneous velocity structure for any location outside the basin.

To visualize possible fault plane reflections, we plotted data points above an ad hoc selected threshold in a cuboid, excluding areas with the strongest artefacts (see Fig. 5b,c and inset in Fig. 6b). The prestack migration steepens the basin's margin compared to the standard poststack migration, and some reflectors appear further east than the first shot point, where 2-D poststack migration could not recover any features. The clearest reflection signal from outside the poststack section migrates to a location 90 m east of shot point 3, at 100–130-m depth. This reflector appears close to the MLF and is marked as FPR (fault plane reflector) in Fig. 1.

4. RESULTS

Combining the shallow tomographic velocity model (Fig. 3) and the reflection image, we obtained a highly resolved image (Fig. 6a) of structural features within the Cheb Basin, with coverage extending to a depth of ≈ 300 m. Relative amplitude recovery is much better in the first half of the survey, while random noise in the stack is boosted between 1500 and 2600 m. The tomographic velocity model has coverage down to ≈ 40 m and shows stronger variations in the high-noise area. In Fig. 3, the velocity model is shown in detail, and color intensity notifies the value of each node's corresponding diagonal element of the resolution matrix. This value is a measure of the linear independence with which each node's velocity was inverted (*Bleibinhaus, 2003*). The tomography's coverage is relatively shallow due to the large velocity gradient and small maximum offsets that were firstly designed for the reflection survey. Still, we resolve important shallow features which are too shallow to be recovered from reflections. Only a small gap in coverage exists between approximately 40–60-m depth between tomographic and reflection images.

The reflection section contains frequencies between 15 and 140 Hz and seismic velocities range between 500 and 1800 m s^{-1}. According to *Sheriff and Geldart (1995)*, reflectors with at least one fourth the minimum wavelength can be recovered in noise-free data, i.e. a minimum of 3 m for this survey. We thus expected to image all major stratigraphic boundaries mentioned in the borehole logs, but not the thinnest beds which are reported down to 1-m thickness in the log for borehole 3870 (*Šantrůček, 1956*). At ≈ 20% error in velocity picking, we estimated the depths of reflectors at a similar accuracy as the difference between the two borehole descriptions suggests (reported basin depths differ by 10 m). Through 3-D Kirchhoff prestack migration, we imaged one steep, but

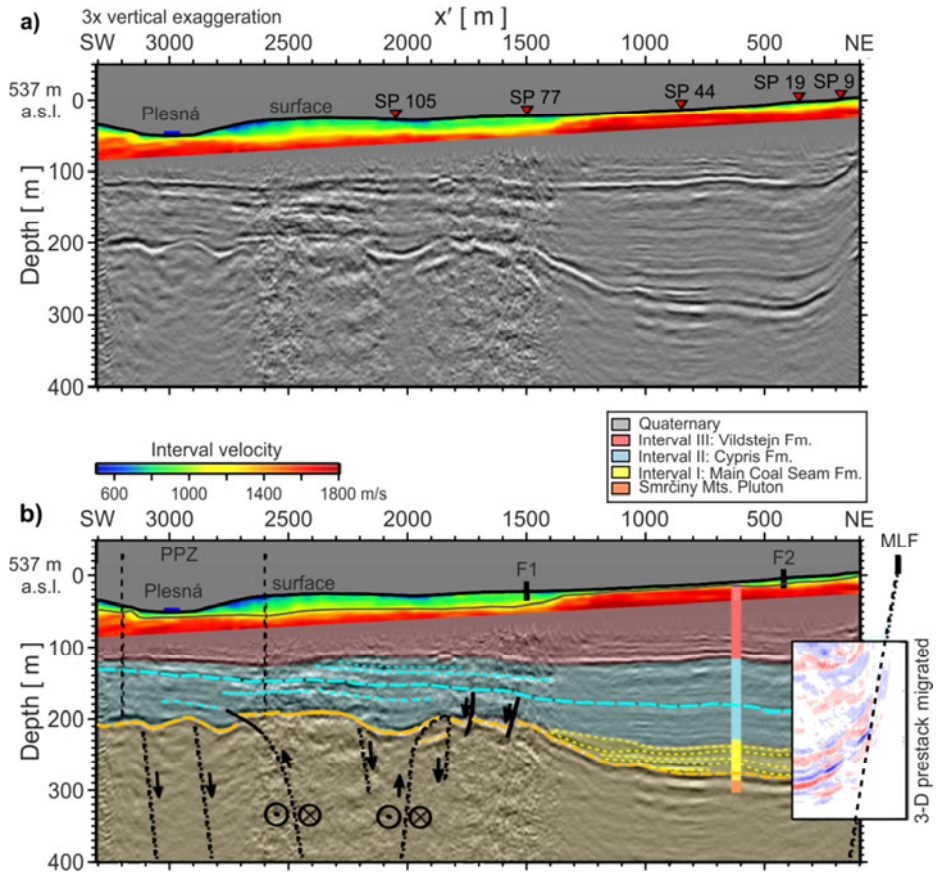

Fig. 6. Reflection seismic image and interpretation. **a)** The poststack depth-migrated image, where the shallowest 40 m are resolved with a tomographic velocity model. **b)** Stratigraphic and structural interpretation of the poststack, prestack and tomographic images. A colored column represents the stratigraphic sequence recorded in close-by boreholes. The Mariánské Lázně Fault (MLF) at the northeastern margin is imaged outside the survey line, shown in the prestack-migrated inset on the right (from Fig. 5). The black dashed lines mark the eastern and western boundaries of the Počátky-Plesná Zone (PPZ) based on *Bankwitz et al., 2003b*), and "F1" and "F2" mark the locations of two faults indicated in Fig. 1, based on *Škvor and Sattran (1974)*. Black lines indicate faulting within the basin, while dotted black lines mark assumed faults within the basement. Arrows indicate these faults' sense of motion, including strike-slip faulting which we deduced from the interpretation of a push-up structure.

weak reflector between 90 and 130-m depth, 90 m from shot point 3, which agrees well with the expected strike and dip of the MLF (*Škvor and Sattran, 1974*; *Bankwitz et al., 2003b*). Connecting the mapped surface outcrop and the reflector's position at depth, we obtained a dip of ≈ 45°, with a large uncertainty due to the resolution of the maps and the weakness of the reflector.

5. DISCUSSION

We interpreted faulting structures, predominantly in the basement, from the migrated section in Fig. 6a and verified main reflectors as major stratigraphic sequences from the boreholes logs (see Fig. 6b).

5.1. Fault structure

Reflectors at the basin floor show multiple disturbances, while intrabasin reflectors appear undisturbed. This change suggests that tectonic activity of faults below the basin must have ceased during the earliest phase of sedimentation in the Cheb Basin. The MLF, adjoining the basin in the NE, is the fault which clearly affected sedimentation along the imaged section the most. Even though our survey did not completely cover it, it is clearly outlined by the upwards bending of reflectors at the eastern margin of the basin. Reflectors widen inside the Main Coal Seam Fm. towards the NE, suggesting progressive subsidence along the MLF. The area closest to the MLF clearly underwent the most subsidence, resulting in the largest sink for sedimentation with a maximum basin depth of ≈ 280 m.

Along the basin floor at 200-m depth between $x' = 1500$ and 3000 m, reflectors terminate and show offsets, suggesting both normal and reverse faults. In the lowermost sediments, the Lower Clay and Sand Fm. and the Main Coal Seam Fm., we observed draped folds at $x' = 3000$ m, depth $z' = 210$ m (described by, e.g., *Sharp et al., 2000*). Such draped folds may form when basement faults are active below sediments with partly ductile behavior, such as clay. Activity along the basement faults must have been limited to the first 5 Myr of basin formation, as succeeding layers appear undisturbed. Simultaneously with the formation of draped folds, reverse faults ($x' = 1900$ m, $z' = 200$ m, and $x' = 2700$ m, $z' = 200$ m) which appear exclusively in the Interval-I sediments must have formed. These reverse faults are visible where the basin floor appears displaced by up to 20 m vertically and where doubled reflectors appear. As there is no record of a compressional regime (*Špičáková et al., 2000*; *Peterek et al., 2011*) within the short history of the Cheb Basin's formation, we explain reverse faults as parts of flower-structures contouring a push-up zone. In the compressional regime between two en-échelon strike-slip faults with the same sinistral sense of motion (marked at $x' = 2000$ m and 2500 m), the enclosed block would have been pushed up.

A parent shear zone to explain the en-échelon faults could be the NNW-SSE striking PPZ as suggested by *Bankwitz et al. (2003b)*, who also described the existence of such faults in the Cheb Basin. *Nickschick et al. (2015)* hypothesized a model of ≈ 200 m wide pull-apart basins at the mofette fields, 4 km south of the survey along the PPZ. While such pull-apart basins would occur at left-stepping en-échelon faults within the parent shear zone with sinistral movement, push-up zones would be expected to form at right-stepping en-échelon faults within the same parent shear zone, the PPZ.

Two small normal faults appear in the lower basin at $x' = 1700$ m, depth $z' = 200$ m, where reflectors are offset by up to 20 m. They are signs of the extensional regime, which enabled the formation of the basin. However, later extension has been accommodated

purely at the MLF, while reflectors (at, e.g., 120-m depth) inside the basin may have been tilted, but not disturbed.

Through 3-D prestack migration, we mapped some steeply dipping reflections close to the basin margin to a location parallel to the MLF (see "FPR" in Fig. 1). According to *Bankwitz et al. (2003b)*, the MLF consists of up to four parallel subfaults within this section, of which some are offset from the main escarpment and appear further west towards the basin. Thus we assume the steeply dipping reflector to be one of the fault planes within the MLF. Borehole S-35 (*Luček, 1962*) towards the south from the FPR hit granite of the Smrčiny Mts. pluton at just 4-m depth, which supports the finding that some faults within the MLF system appear further within the basin than the escarpment might suggest. We image the fault plane reflector at a dip of $\approx 45°$ (in MVE survey: 57°, *Bleibinhaus et al., 2003*), but our estimate lacks accuracy because of the weak signal.

5.2. Stratigraphy and basin evolution

There is a good fit between reported depths of the main stratigraphic boundaries in logs of boreholes SŠ-4 and 3870 (*Šantrůček, 1956*; *Plaček, 1966*) which are located less than 25 m from the survey line close to $x' = 600$ m, and major reflections in the migrated section. The four main reflectors between 110 and 280-m depth and their associated sediment intervals are listed in Table 1.

The Main Coal Seam Fm. is foremost present in the deep trough at the NE margin of the basin, where localized sedimentation occured (*Špičáková et al., 2000*). Here, its layers downlap and widen towards the MLF, showing gradual opening of the basin along the MLF during the Miocene. Layers of the formation thin out towards the SW, where they onlap the SE margin of the trough. Simultaneously, normal faulting at preexistent basement faults led to draped folds appearing in the basin's layers when the clay-rich layers were bended by vertical movement along the faults. On sections with better amplitude preservation (no AGC), bright spots clearly appear in the synclines of draped folds ($x' = 2800$ m and $x' = 3100$ m at $z' = 200$ m). These spots might indicate that fluid is accumulated in the synclines, e.g. groundwater in sand between clayey, impermeable layers. *Bankwitz et al. (2003a)* described that the main acquifer lies right below the Vildštejn Fm., but clayey beds may well form impermeable barriers to deeper sandy layers.

In late Miocene to early Pliocene (21–17 Ma), further subsidence due to high activity at the MLF offered ample space for sedimentation of the Cypris Fm. across the whole basin (*Špičáková et al., 2000*). These layers (at, e.g., 120-m depth) are tilted towards the NE with little long-wavelength topography and are unaffected by faulting. Reflectors of the Vildštejn Fm. are horizontal, marking an unconformity (*Špičáková et al., 2000*; *Schunk et al., 2003*; *Peterek et al., 2011*) above erosionally truncated layers of the Cypris Fm. sediments.

At the bottom of the Vildštejn Fm., an amplitude reversal at 120-m depth at $x' = 1850$ m might indicate a paleo-channel of the Plesná river. At first glance, this amplitude reversal might look conspicuous, as it appears above the location where we interpreted possible faulting within the basement. These features are, however, no processing artefacts, which the following characteristics support: 1) The amplitude reversal is accompanied by increased amplitudes and already appears in the unmigrated

stack, before phase correction for stack power maximization are introduced. 2) Weaker, but clear reflectors within the Cypris Fm. show no disturbance across this area. 3) The offset across the basin floor is three to four times larger than the offset at the amplitude reversal.

None of the reflectors within the basin show significant offsets, but some peculiarities appear which suggest fluid migration. Indications for fluids are the high amplitudes in synclines and the disturbed zone at $x' = 2600$ m. This disturbed zone might be caused by distributed fluid migration, comparable to how the mofette field Milhostov-Hartoušov emanates CO_2-rich gas in several small mofettes.

5.3. Quaternary deposits

The thickness of Quaternary sediments was reported to be between 3 and 4 m for the two boreholes next to our survey at $x' = 600$ m. Our reflection seismic image cannot recover such a shallow structure, but we can resolve such structure from the tomographic velocity model. Close to the borehole locations, we image a thin, shallow layer of very slow seismic velocities ($v_P < 800$ m s^{-1}) which fall into the range expected for unconsolidated sand (250–1000 m s^{-1}, *Prasad et al., 2004*). Closer towards the Plesná valley, but still on its eastern plateau, these very slow velocities reach down to 25 m. This is in agreement with the thickness of Quaternary sand deposits stated by *Flechsig et al. (2010)* for borehole VD-121, which is located approximately 170 m off the seismic survey at $x' = 2500$ m. Borehole VD-14 (*Čermák and Kašák, 1959*), approximately 100 m further west than the SW end of our survey shows Quaternary sand deposits of only 4-m thickness. Towards this borehole, the isoline of 1200 m s^{-1} trends upwards again, suggesting that also here the isoline could fit the thickness of Quaternary sands. The clear step in slow velocity thickness at $x' = 1400$ m in Fig. 3 coincides with a fault marked on the geologic map of *Škvor and Sattran (1974)*, suggesting that they observed a contrast at the surface.

At the Bublák mofette field 1500 m downstream the Plesná river, *Hubatka et al. (2004)* imaged nearly undisturbed sandy layers with an average thickness of 9 m, at most 12-m thickness close to the river in a ground penetrating radar (GPR) study. In this location, the sandy layers thin to ≈ 5 m at a distance of 100–200 m from the Plesná river. The sharp change in electric and lithological properties would fit our interpretation of a strong velocity gradient that shows the top of the Vildštejn Fm. Under this assumption, the tomographic image shows a structure similar to that at Bublák, where Quaternary sediments are deposited in an area limited by steps at the top of the Vildštejn Fm. We explain these pronounced steps with the erosion of and deposition on fluvial terraces, whose existence *Schunk et al. (2003)* suggested for the basin.

Špičáková et al. (2000) and *Peterek et al. (2011)*, agree that an erosional discordance separates the Vildštejn Fm. and Quaternary sediments. Hence, we suspect that the Plesná river eroded parts of the Vildštejn Fm. in an erosional terrace, where deposition of Quaternary, unconsolidated and seismically slow sediments centered afterwards. Today's river bed was incised into Quaternary sediments and rests closely above the Vildštejn layers, forming the escarpement on the eastern river bank.

6. CONCLUSIONS

Our seismic reflection image of the North-Eastern Cheb Basin shows the detailed structure of an up to 300-m thick sedimentary basin over crystalline basement. The top of the basement is strongly faulted, including normal faults related to the initial stages of basin formation, and reverse faults, probably related to a push-up structure from sinistral strike-slip motion along the Počátky-Plesná zone (PPZ). The interpreted stratigraphy is consistent with nearby boreholes and geologic models. The reflection image shows the three major formations (Coal Seam, Cypris, Vildštejn Fm.) separated by distinct reflection horizons. One finding that surprised us is the complete absence of faulting in the sedimentary strata. This indicates that during the major stage of basin formation, basement faulting ceased, and all extension was accommodated further to the NE, at the basin-bounding Mariánské Lázně Fault (MLF). This is also seen from the progressive thickening of the strata towards the MLF. In addition, our results show that the escarpment at the Plesná river bank is not related to normal faulting at the PPZ. A conspicuous zone of low amplitudes could indicate a vertical fluid pathway similar to the one that feeds the mofette fields Milhostov-Hartoušov.

Acknowledgements: We would like to acknowledge Christina Flechsig and two other anonymous reviewers for constructive comments and suggestions that helped improve the article. The seismic data were acquired in 2013 as part of the applied geophysics field camp of Friedrich-Schiller-University Jena, and we would like to thank Kamil Ustaszewski for helpful remarks about the seismic interpretation. Figures 1 and 4–6 were partly or completely generated with the Generic Mapping Tools (GMT, Wessel et al., 2013).

References

Adamovič J. and Coubal M., 1999. Intrusive Geometries and Cenozoic Stress History of the Northern Part of the Bohemian Massif. *GeoLines*, **9**, 5–14.

Babuška V., Plomerová J. and Fischer T., 2007. Intraplate seismicity in the western Bohemian Massif (central Europe): a possible correlation with a paleoplate junction. *J. Geodyn.*, **44**, 149–159, DOI: 10.1016/j.jog.2007.02.004.

Bancroft J.C., 2007. *A Practical Understanding of Pre- and Poststack Migrations*. Volume 1. Society of Exploration Geophysicists, Tulsa, OK.

Bankwitz P., Bankwitz E., Bräuer K., Kämpf H. and Störr M., 2003a. Deformation structures in Plio-and Pleistocene sediments (NW Bohemia, central Europe). *Geol. Soc. London Spec. Publ.*, **216**, 73–93.

Bankwitz P., Schneider G., Kämpf H. and Bankwitz E., 2003b. Structural characteristics of epicentral areas in Central Europe: Study case Cheb Basin (Czech Republic). *J. Geodyn.*, **35**, 5–32.

Bleibinhaus F., 2003. *3D Simultaneous Refraction and Reflection Seismic Travel Time Tomography and Application to Deep Seismic TRANSALP Wide-Angle Data*. PhD Thesis, Ludwig-Maximilians-Universität, München, Germany.

Bleibinhaus F., Stich D., Simon M. and Gebrande H., 2003. New results from amplitude preserving prestack depth migration of the Münchberg/Vogtland segment of the MVE deep seismic survey. *J. Geodyn.*, **35**, 33–43.

Bräuer K., Kämpf H., Niedermann S., Strauch G. and Tesař J., 2008. Natural laboratory NW Bohemia: Comprehensive fluid studies between 1992 and 2005 used to trace geodynamic processes. *Geochem. Geophys. Geosyst.*, **9**, Q04018, DOI: 10.1029/2007GC001921.

Bucha V., Horáček J. and Malkovský M., 1990. Paleomagnetic stratigraphy of the Tertiary of the Cheb Basin (W.Bohemia). *Věstník Ústředního ústavu geologického*, **65**, 267–278 (in Czech).

Čermák J. and Kašák F., 1959. *Geological Description of Object VD-14*. Technical Report. Czech Geological Survey - GEOFOND Database of Geologically Described Objects, Prague, Czech Republic.

DEKORP Research Group, 1994a. Profile DEKORP 3/MVE-90: reflection seismic field measurements and data processing. *Z. Geol. Wiss.*, **22**, 631–646.

DEKORP Research Group, 1994b. Crustal structure of the Saxothuringian Zone: Results of the deep seismic profile MVE-90(East). *Z. Geol. Wiss.*, **22**, 647–769.

Dix C.H., 1955. Seismic velocities from surface measurements. *Geophysics*, **20**, 68–86, DOI: 10.1190/1.1438126.

Eberhart-Phillips D., 1990. Three-dimensional P and S velocity structure in the Coalinga region, California. *J. Geophys. Res.*, **95**, 15343–15363. DOI: 10.1029/JB095iB10p15343.

Emmert U., Horstig G. and Stettner G., 2007. *Geologische Übersichtskarte 1:200.000, CC 6334 Bayreuth*. Bundesanstalt für Geowissenschaften und Rohstoffe, Hannover, Germany (in German).

Fischer T. and Michálek J., 2008. Post 2000-swarm microearthquake activity in the principal focal zone of West Bohemia/Vogtland: space-time distribution and waveform similarity analysis. *Stud. Geophys. Geod.*, **52**, 493–511.

Fischer T., Horálek J., Michálek J. and Boušková A., 2010. The 2008 West Bohemia earthquake swarm in the light of the WEBNET network. *J. Seismol.*, **4**, 665–682.

Fischer T., Štěpančíková P., Karousová M., Tábořík P., Flechsig C. and Gaballah M., 2012. Imaging the Mariánské Lázně Fault (Czech Republic) by 3-D ground penetrating radar and electric resistivity tomography. *Stud. Geophys. Geod.*, **56**, 1019–1036, DOI: 10.1007/s11200-012-0825-z.

Fischer T., Horálek J., Hrubcová P., Vavryčuk V., Bräuer K. and Kämpf H., 2014. Intracontinental earthquake swarms in West-Bohemia and Vogtland: A review. *Tectonophysics*, **611**, 1–27, DOI: 10.1016/j.tecto.2013.11.001.

Flechsig C., Fabig T., Rücker C. and Schütze C., 2010. Geoelectrical investigations in the Cheb Basin/W-Bohemia: an approach to evaluate the near-surface conductivity structure. *Stud. Geophys. Geod.*, **54**, 443–463.

Hole J.A., Thybo H. and Klemperer S.L., 1996. Seismic reflections from the near-vertical San Andreas Fault. *Geophys. Res. Lett.*, **23**, 237–240.

Hole J.A., Catchings R.D., St Clair K.C., Rymer M.J., Okaya D.A. and Carney B.J., 2001. Steep-dip seismic imaging of the shallow San Andreas fault near Parkfield. *Science*, **294**, 1513–1515, DOI: 10.1126/science.1065100.

Hubatka F., Boušková A., Špičák A., Švancara J. and Tilšarová R., 2004. Ground penetrating radar profile measurements above the seismoactive area at the Eastern margin of the Cheb Basin, Western Bohemia. *GeoLines*, **17**, 41–42.

Kolářová M., 1965. Hydrogeologie chebské pánve (Hydrogeology of the Cheb Basin). *Sborník Geologických Věd*, *Hydrogeologie a Inženýrská Geologie*, **3**, 7–101. Ústřední Ústav Geologický, ÚÚG, (Czech Geological Survey) Prague, Czech Republic (in Czech).

Luček J., 1962. *Geological Description of Object S-35*. Technical Report, Czech Geological Survey-GEOFOND Database of Geologically Described Objects, Prague, Czech Republic.

Malkovský M., 1987. The Mesozoic and Tertiary basins of the Bohemian Massif and their evolution. *Tectonophysics*, **137**, 31–42.

Mrlina J., Kämpf H., Kroner C., Mingram J., Stebich M., Brauer A., Geissler W.H., Kallmeyer J., Matthes H. and Seidl M., 2009. Discovery of the first Quaternary maar in the Bohemian Massif, Central Europe, based on combined geophysical and geological surveys. *J. Volcanol. Geotherm. Res.*, **182**, 97–112, DOI: 10.1016/j.jvolgeores.2009.01.027.

Nickschick T., Kämpf H., Flechsig C., Mrlina J. and Heinicke J., 2015. CO2 degassing in the Hartousov mofette area, western Eger Rift, imaged by CO2 mapping and geoelectrical and gravity surveys. *Int. J. Earth Sci.*, **104**, 2107–2129, DOI: 10.1007/s00531-014-1140-4.

Peterek A., Reuther C.-D. and Schunk R., 2011. Neotectonic evolution of the Cheb Basin (Northwestern Bohemia, Czech Republic) and its implications for the late Pliocene to recent crustal deformation in the western part of the Eger Rift. *Z. Geol. Wiss.*, **39**, 335–365.

Plaček Z., 1966. *Geological Description of Object 3870*. Technical Report. Czech Geological Survey - GEOFOND Database of Geologically Described Objects, Prague, Czech Republic.

Prasad M., Zimmer M.A., Berge P.A. and Bonner B.P., 2004. *Laboratory Measurements of Velocity and Attenuation in Sediments*. Technical Report UCRL-JRNL-205155. Society of Exploration Geophysicists, Tulsa, OK.

Ristow D. and Rühl T., 1994. Fourier finite-difference migration. *Geophysics*, **59**, 1882–1893.

Ronen J. and Claerbout J.F., 1985. Surface-consistent residual statics estimation by stack-power maximization. *Geophysics*, **50**, 2759–2767.

Šantrůček P., 1956. *Geological Description of Object SŠ-4*. Technical Report. Czech Geological Survey - GEOFOND Database of Geologically Described Objects, Prague, Czech Republic.

Scherbaum F., 2001. *Of Poles and Zeros*. 2nd Edition. Springer, Dordrecht, The Netherlands, DOI: 10.1007/978-1-4020-6861-4.

Schleicher K., 2012. *Open Data/Open Source: Seismic Unix Scripts to Process a 2D Land Line*. Technical Report. The University of Texas at Austin, Austin, TX.

Schunk R., Peterek A. and Reuther C., 2003. Untersuchungen zur quartären und rezenten Tektonik im Umfeld der Marienbader Störung und des Egerer Beckens (Tschechien) – erste Ergebnisse (Investigations into the Quaternary and Recent Tectonics of the area around the Marianske Lazne Fault and of the Cheb). *Mitt. Geol.-Paläont. Inst. Univ. Hamburg*, **87**, 19–46 (in German).

Sharp I.R., Gawthorpe R.L., Underhill J.R. and Gupta S., 2000. Fault-propagation folding in extensional settings: Examples of structural style and synrift sedimentary response from the Suez rift, Sinai, Egypt. *Bull. Geol. Soc. Am.*, **112**, 1877–1899.

Sheriff R.E. and Geldart L., 1995. *Exploration Seismology*. 2nd Edition. Cambridge University Press, Houston, TX.

Škvor V. and Sattran V., 1974. *Krušné Hory, západní část (The Ore Mountains, Western Part)*. 1:50.000 (Geological Map of Czech Republic), 11–14, Czech Geological Survey, Prague, Czech Republic.

Špičáková L., Uličný D. and Koudelková G., 2000. Tectonosedimentary evolution of the Cheb Basin (NW Bohemia, Czech Republic) between late Oligocene and Pliocene: a preliminary note. *Stud. Geophys. Geod.*, **44**, 556–580.

Stockwell J.W. and Cohen J.K., 2008. *The New SU User's Manual*. Technical Report, Colorado School of Mines, Golden, CO.

Thurber C.H., 1983. Earthquake locations and three-dimensional crustal structure in the Coyote Lake Area, central California. *J. Geophys. Res.*, **88**, 8226, DOI: 10.1029/JB088iB10p08226.

Thurber C.H. and Eberhart-Phillips D., 1999. Local earthquake tomography with flexible gridding. *Comput. Geosci.*, **25**, 809–818, DOI: 10.1016/S0098-3004(99)00007-2.

Weinlich F.H., Faber E., Boušková A., Horálek J., Teschner M. and Poggenburg J., 2006. Seismically induced variations in Mariánské Lázně fault gas composition in the NW Bohemian swarm quake region, Czech Republic - A continuous gas monitoring. *Tectonophysics*, **421**, 89–110, DOI: 10.1016/j.tecto.2006.04.012.

Wessel P., Smith W.H.F., Scharroo R., Luis J. and Wobbe F., 2013. Generic Mapping Tools: Improved version released. *EOS Trans. AGU*, **94(45)**, 409–410, DOI: 10.1002 /2013EO450001.

Yilmaz O., 2001. *Seismic Data Analysis: Processing, Inversion, and Interpretation of Seismic Data*. Society of Exploration Geophysicists, Tulsa, OK.